Engineering Structures 220 (2020) 110920

Contents lists available at ScienceDirect

Engineering Structures

journal homepage: www.elsevier.com/locate/engstruct

Numerical evaluation of a novel passive variable friction damper for vibration mitigation

Vahid Barzegar[a,*], Simon Laflamme[a,b], Austin Downey[c,d], Meng Li[e], Chao Hu[b,e]

[a] Department of Civil, Construction, and Environmental Engineering, Iowa State University, Ames, IA, USA
[b] Department of Electrical and Computer Engineering, Iowa State University, Ames, IA, USA
[c] Department of Mechanical Engineering, University of South Carolina, Columbia, SC, USA
[d] Department of Civil and Environmental Engineering, University of South Carolina, Columbia, SC, USA
[e] Department of Mechanical Engineering, Iowa State University, Ames, IA, USA

ARTICLE INFO

Keywords:
Variable friction
Structural control
Passive friction
Vibration mitigation
Wind
Seismic

ABSTRACT

This study assesses the performance of a novel passive variable friction damper (PVFD) at mitigating wind- and seismic-induced vibrations. The PVFD consists of two friction plates upon which a cam profile modulates the normal force as a function of its rotation. A unique feature of the PVFD is its customizable shape, yielding a customizable friction hysteresis. The objective of the study is to assess the benefits of crafting the friction behavior to satisfy motion criteria. This is done numerically on two example buildings: a 5-story structure subjected to seismic loads, and a 20-story structure subjected to non-simultaneous seismic and wind loads. A probabilistic performance-based design procedure is introduced to select the optimum cam configurations throughout each building under the design loads. After that, numerical simulations are conducted to compare their performance against that of two equivalent damping schemes: viscous dampers and passive friction dampers. Results show that customization of the hysteresis behaviors throughout a structure is necessary to yield optimal performance. Also, the PVFD outperforms the other damping schemes for wind mitigation by yielding a more stable response in terms of lower accelerations over the entire wind event. Under seismic loads, all three damping schemes exhibited comparable performance, but the PVFD yielded a significantly more uniform drift for the 20-story building.

1. Introduction

Supplemental damping in structures can be achieved through the installation of passive, semi active, and active damping systems, enabling structures to attain higher motion-based performance criteria [1]. Among them, passive supplemental damping systems have been widely accepted by the structural engineering field due to their demonstrated long term reliability and cost-effectiveness [2–4]. Examples of passive devices include viscous dampers [5,6], viscoelastic dampers [7,8], metallic and friction dampers [9–11], tuned mass/fluid dampers [12–14], and base isolation systems [15–17].

Of interest to this paper are friction dampers, typically characterized by mechanical simplicity, loading rate independency, and large energy dissipation capabilities [18]. These devices dissipate mechanical vibrations into heat through the sliding of one or many surfaces. Several types of friction devices have been proposed in the literature. In early works, Pal et al. [19] proposed the integration of sliding surfaces lined with brake pads to reduce the kinetic energy of braced frames. Later, Mualla et al. [20] studied the use of two friction pad disks sandwiched between three concentric steel plates installed in a hinge connection. Morgan et al. [21] added friction dampers to the beam-column connection of post-tensioned precast frame structures to leverage the gap opening of the connections for energy dissipation. Wolski et al. [22] adopted a similar principle to steel moment-resisting frame connections. The bottom flange of the beam was connected to the column through long slotted holes supported by post-tensioned strands to add self-centering capability. When the applied moment surpassed the tension in the strands, the connection plates slid and dissipated energy.

The challenge with the aforementioned passive friction dampers is overcoming the static friction force. When the activation force of the damper is too large, the sliding parts will not move under moderate and low excitations, resulting in the device acting as a stiffness element. On the other hand, with small activation forces, the sliding interfaces will not be effective. To address this limitation, some researchers have

* Corresponding author.
E-mail address: barzegar@iastate.edu (V. Barzegar).

https://doi.org/10.1016/j.engstruct.2020.110920
Received 24 December 2019; Received in revised form 15 May 2020; Accepted 1 June 2020

proposed optimization algorithm to obtain an optimum activation force over the height of the buildings [23–25]. Also, several damping systems have been proposed to modulate the normal force of the friction damper through an external force input, termed variable friction devices [18,26–28]. Closer to the work presented in this paper, researchers have also proposed passive variable friction devices (PVFDs), where the friction force of a passive friction damper is a function of displacement. For example, Pancha et al. [29] proposed a friction base isolator incorporating a spherical sliding surface with varying roughness. Calvi et al. [30] developed a similar isolation device consisting of a circular slider on flat concentric rings of different friction coefficients. Instead of varying the coefficient of friction, Wang et al. [31] developed a damper termed arc-surfaced frictional damper where the normal force varies with the sliding of a friction element within an arc-shaped tube. Bagheri et al. [32] introduced and experimentally tested a self-centering friction joint with triangular corrugated friction plates. The relative movement of the corrugated plates increased the compression on the sliding surfaces and hence increased the friction force.

The authors have recently studied a type of PVFD [33] in which the normal force on the friction pads is modulated by a cam as a function of displacement. Through this mechanism, one can strategically configure the hysteresis behavior of the device to optimize vibration mitigation. The PVFD has been characterized in a laboratory at the individual device level [33]. This paper extends the previous work on the PVFD by numerically studying its potential at mitigating natural hazards. In particular, the performance of the device is studied on a 20-story building subjected to seismic or wind excitations, and on a 5-story building subjected to seismic excitations. A motion-based design procedure to optimize the design of individual hysteresis is presented, which consists of iteratively designing groups of devices that minimize the response variance. The value in customizing individual hysteresis loops is also investigated by comparing the performance of the device against conventional passive friction devices (PFDs).

The rest of the paper is organized as follows. Section 2 introduces the PVFD and its modeling. Section 3 describes the research methodology including the description of the prototype buildings, loads, and the PVFD design. Section 4 provides the results of simulations of the prototype buildings equipped with the PVFD. Section 5 summarizes the conclusions of this study.

2. Passive variable friction device

The PVFD is a cam-based passive friction device capable of generating customized hysteresis behaviors through a cam profile. It is composed of two sliding friction plates upon which the cam produces a profile-dependent variable pressure, therefore generating a variable normal force. A schematic of the device and the installation configuration in the building frame are illustrated in Fig. 1 (a) and (b), respectively. The cam is engineered to allow for a quick update of the supplemental energy dissipation system by simply changing the cam itself, which is a net advantage over conventional passive friction devices (PFDs). This can be particularly helpful to adapt the structural behavior to new, unforeseen loads, such as those provoked by a changes in climate and cityscape. The cam is connected to the upper and lower friction plates through rigid linkages. The friction plates are clamped between the frame and the cam at $\theta = 0$ to provide a preloading force $F_{N,\text{preload}}$. A relative motion between the beam and the bracings along y provokes a reactive damping force F_d and a rotation θ in the cam that supplements the total normal force F_N acting on the friction plates by $F_{N,\text{cam}}$.

$$F_{N,\text{cam}}(\theta) = k\Delta r(\theta) \tag{1}$$

with $F_{N,\text{cam}} = 0$ at $\Delta r(0) = 0$, and where k is the vertical stiffness of the device and $\Delta r(\theta)$ is the change in the radius provoked by a rotation θ with respect to the radius at $\theta = 0$.

The total normal force F_N acting on the friction plates consists of the preloading force $F_{N,\text{preload}}$ and the added cam-induced force $F_{N,\text{cam}}$

$$F_N(\theta) = F_{N,\text{preload}} + F_{N,\text{cam}}(\theta) \tag{2}$$

A Coulomb friction model is used to estimate the kinetic damping force $F_{\text{kinetic}}(\theta)$

$$F_{\text{kinetic}}(\theta) = \nu F_N(\theta) \tag{3}$$

where ν is the coefficient of kinetic friction with a value of 0.4 in this study based on the material used in fabricating the prototype device in [33]. In this study, an elliptical cam shape is used, which provides a smooth change in the normal force. Based on the equation of an ellipse in polar coordinates, the radius of the cam, r, acting on the friction plates can be derived as

$$r(\theta) = \frac{ab}{\sqrt{a^2\sin^2\left(\theta - \frac{\pi}{2}\right) + b^2\cos^2\left(\theta - \frac{\pi}{2}\right)}} \tag{4}$$

where a and b are the axes of the ellipse, respectively, as illustrated in Fig. 1. The rotation of the cam can also be related to the relative displacement of the friction pads as

$$\theta = \tan^{-1}\left(\frac{y}{d}\right) \tag{5}$$

where d is the distance between the two holes of the cam annotated in Fig. 1.

The dynamic behavior of a PVFD prototype was previously characterized using a modified LuGre friction model [33]. The dynamic friction force F_d is written as

$$F_d = \sigma_0 z + \sigma_1 \dot{z} + \sigma_2 \dot{y} \tag{6}$$

with

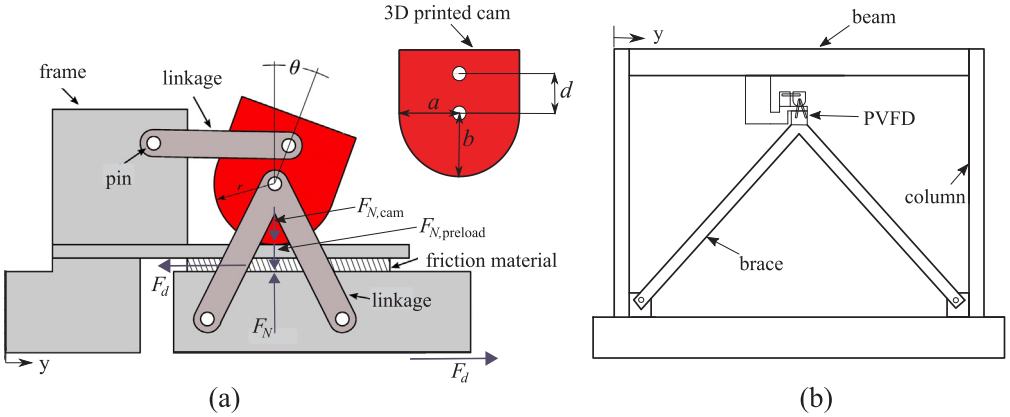

Fig. 1. (a) Schematic representation of the PVFD [33]; and (b) an example of its installation in a braced frame.

Table 1
Parameters of the LuGre model [33].

σ_0 (N/m)	σ_1 (N·s/m)	σ_2 (N·s/m)	$\dot{y}_s$ (m/s)
2.605×10^6	826	1049	0.001

$$\dot{z} = \dot{y} - \sigma_0 \frac{|\dot{y}|}{g(\dot{y})} z \tag{7}$$

$$g(\dot{y}) = \left(F_{\text{static}} - F_{\text{kinetic}}\right) \exp\left(-\left(\frac{\dot{y}}{\dot{y}_s}\right)^2\right) \tag{8}$$

where F_{static} is the static friction force taken as 1.02 times the kinetic force [33], σ_0, σ_1, and σ_2, are constant values describing the stiffness of the bristles, micro-displacement damping, and viscous friction, respectively, z is an evolutionary variable, $\dot{y}$ is the relative velocity of friction plates, $g(\dot{y})$ is a function describing the Stribeck effect, and $\dot{y}_s$ is a constant representing the Stribeck velocity. Table 1 lists the parameters of the LuGre model characterized through an experimental prototype of the device in [33].

Fig. 2 plots the hysteresis behavior of five example PVFDs using Eqs. (1)–(8) for the geometric parameters listed in Table 2. These force–displacement and force–velocity loops were produced under a harmonic excitation of amplitude 10 mm at 0.2 Hz using the LuGre friction model. The hysteresis loops illustrate that the PVFD is highly customizable.

3. Methodology

The performance of the PVFD at mitigating vibrations at the building level is numerically investigated on two prototype structures. The first one is a 5-story building subjected to seismic loads, and the second one is a 20-story building subjected to wind or seismic loads. In what follows, the numerical models of the buildings are discussed, followed by a description of the external loads and control strategies studied.

3.1. Prototype buildings

Numerical simulations are conducted on a 5-story and a 20-story building. The 5-story building is a structure located in Shizuoka City, Japan, and studied in literature [34,35]. The 20-story building is a structure located in Los Angeles, CA, previously used as a benchmark control problem [36]. Both buildings are simulated as lumped-mass shear buildings in their shorter direction. The first three natural periods of the buildings are listed in Table 3. The model parameters of the 5-story and 20-story buildings are listed in Tables 4 and 5, respectively. The inherent first modal damping ratio of both buildings is assumed to

Table 2
Parameters of the PVFD prototype [33].

	Cam				
Parameter	1	2	3	4	5
a (mm)	29.3	30.4	31.5	32.6	33.7
b (mm)	31.5	31.5	31.5	31.5	31.5
d (mm)	28	28	28	28	28
F_{preload} (kN)	0.7	0.7	0.7	0.7	0.7

Table 3
Natural periods of the prototype buildings.

	Period (s)	
mode	5-story	20-story
1	0.991	3.78
2	0.345	1.37
3	0.223	0.83

Table 4
Model parameters of the 5-story building.

Floor	Height (m)	Mass (10^3 kg)	Stiffness (kN/m)
1	4.2	215.2	147000
2	3.6	209.2	113000
3	3.6	207.0	99000
4	3.6	204.8	89000
5	3.6	266.1	84000

Table 5
Modeling parameters of the 20-story building.

Floor	Height (m)	Mass (10^3 kg)	Stiffness (kN/m)	Floor	Height (m)	Mass (10^3 kg)	Stiffness (kN/m)
1	5.49	563	225,568	11	3.96	552	244,832
2	3.96	552	304,192	12	3.96	552	236,096
3	3.96	552	299,712	13	3.96	552	232,064
4	3.96	552	297,920	14	3.96	552	203,392
5	3.96	552	275,072	15	3.96	552	200,928
6	3.96	552	279,552	16	3.96	552	197,568
7	3.96	552	277,088	17	3.96	552	178,752
8	3.96	552	273,952	18	3.96	552	164,416
9	3.96	552	270,592	19	3.96	552	133,952
10	3.96	552	265,888	20	3.96	584	100,576

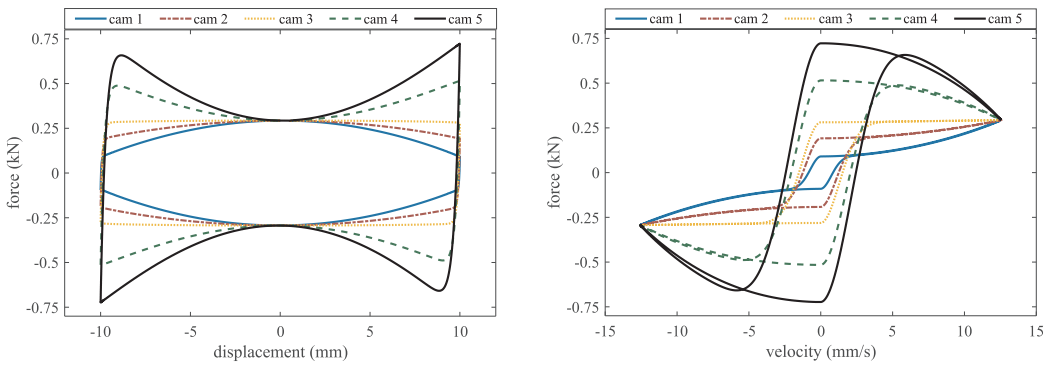

Fig. 2. Dynamic behavior of the PVFD with different geometric parameters under harmonic excitation: (a) force–displacement loops; and (b) force–velocity loops.

be 2%, with damping assumed to be proportional to the stiffness matrix of the structures [1].

A state-space formulation is used to model and simulate the buildings. Consider the equation of motion for an n degree-of-freedom structure equipped with supplemental damping devices

$$\mathbf{M}\ddot{\mathbf{U}} + \mathbf{C}\dot{\mathbf{U}} + \mathbf{K}\mathbf{U} + \mathbf{E}_d\mathbf{F}_d = -\mathbf{M}\mathbf{E}a_g + \mathbf{E}_f\mathbf{F}_w \tag{9}$$

where $\mathbf{M}, \mathbf{C}, \mathbf{K}$ are mass, damping, and stiffness matrices of the building, respectively, $\mathbf{F}_d$ is the damping devices force vector, $\mathbf{U}$ is the building displacement vector, the dot denotes a time derivative, $\mathbf{F}_w$ is the wind load vector, a_g is the ground acceleration input, and $\mathbf{E}_d$, $\mathbf{E}$ and $\mathbf{E}_f$ are damping devices, the ground acceleration and wind load input location matrices, respectively. The state space representation of the equation of motion is written as

$$\dot{\mathbf{X}} = \mathbf{A}\mathbf{X} + \mathbf{B}_d\mathbf{F}_d + \mathbf{B}_f\mathbf{F}_w + \mathbf{B}_g a_g \tag{10}$$

with

$$\mathbf{X} = \begin{bmatrix}\mathbf{U}\\ \dot{\mathbf{U}}\end{bmatrix} \quad \mathbf{A} = \begin{bmatrix}\mathbf{0} & \mathbf{I}\\ -\mathbf{M}^{-1}\mathbf{K} & -\mathbf{M}^{-1}\mathbf{C}\end{bmatrix} \quad \mathbf{B}_d = \begin{bmatrix}\mathbf{0}\\ -\mathbf{M}^{-1}\mathbf{E}_d\end{bmatrix} \quad \mathbf{B}_f = \begin{bmatrix}\mathbf{0}\\ \mathbf{M}^{-1}\mathbf{E}_f\end{bmatrix} \quad \mathbf{B}_g = \begin{bmatrix}\mathbf{0}\\ -\mathbf{E}\end{bmatrix} \tag{11}$$

where $\mathbf{X}$ is the state vector, $\mathbf{A}$ is the state matrix, and $\mathbf{B}_d$, $\mathbf{B}_f$ and $\mathbf{B}_g$ are the input vectors. A discrete time formulation as discussed in reference [1] is used to solve the state-space equation. Assuming known state at time step j, the state of the system at time step $j+1$ is approximated as

$$\mathbf{X}_{j+1} = \mathrm{e}^{\mathbf{A}\Delta t}\mathbf{X}_j + \mathbf{A}^{-1}(\mathrm{e}^{\mathbf{A}\Delta t} - \mathbf{I})[\mathbf{B}_g a_{g,j} + \mathbf{B}_f\mathbf{F}_j] \tag{12}$$

where e and $\mathbf{I}$ are the exponential function and identity matrix, respectively. The prototype buildings are simulated and analyzed in MATLAB (Release 2017a).

3.2. External loads

The selected structures are excited under non-simultaneous seismic and wind events.

Wind loads are simulated as concentrated forces acting at each floor level. The wind force acting on a floor level at height z is simulated as [37]

$$F_w\left(z, t\right) = \frac{1}{2}\rho V^2\left(z, t\right)AC_D \tag{13}$$

where ρ is the air density, A is the area exposed to the wind pressure, C_D is the drag coefficient of the structure, and V is the wind speed consisting of two components

$$V(z, t) = \overline{V}(z) + v(z, t) \tag{14}$$

with $\overline{V}$ as the mean wind speed and v as the zero mean fluctuating component. The value of $\overline{V}$ is determined from a 3-s gust speed $\overline{V}_0$ obtained from hazard maps. Value $\overline{V}_0$ is the mean speed of wind for an open terrain at 10 m, and is modified for different terrains and heights using [37]

$$\overline{V}(z) = \overline{V}_0^{\text{terrain}}\frac{\ln(z/z_*)}{\ln(10/z_*)} \tag{15}$$

with

$$\overline{V}_0^{\text{terrain}} = \overline{V}_0\frac{\nu_*}{\nu_{*0}}\frac{\ln(10/z_*)}{\ln(10/z_{*0})} \tag{16}$$

where $\overline{V}_0^{\text{terrain}}$ is the mean velocity of wind for a given terrain, ν_* and ν_{*0} are the shear velocities of the building site and open terrain, respectively, and z_* and z_{*0} are the surface roughness for the building site and open terrain, respectively.

The fluctuating component $v(z, t)$ is simulated as a multi-variate stochastic process with cross-spectral density matrix given by [38]

$$S_{ij} = \begin{cases} S_k(z_i, \omega) & i = j \\ \sqrt{S_k(z_i, \omega)S_k(z_j, \omega)}\,C_{ij}(\omega) & i \neq j \end{cases} \tag{17}$$

where S_k is the Kaimal power spectral density function of the longitudinal wind velocity fluctuations at excitation frequency ω and height z

$$S_k\left(z, \omega\right) = \frac{1}{2}\frac{200}{2\pi}\nu_*^2\frac{z}{\overline{V}(z)}\frac{1}{\left(1 + 50\frac{\omega z}{2\pi\overline{V}(z)}\right)^{\frac{5}{3}}} \tag{18}$$

and C_{ij} is the coherence function between fluctuations at heights i and j

$$C_{ij}(\omega) = \exp\left(-\frac{\omega}{2\pi}\frac{10\Delta z}{\frac{1}{2}(\overline{V}(z_i) + \overline{V}(z_j))}\right) \tag{19}$$

The cross-spectral density matrix is decomposed in order to obtain values at different heights using Cholesky's decomposition

$$\mathbf{S}(\omega) = \mathbf{H}(\omega)\mathbf{H}^{*T}(\omega) \tag{20}$$

where $\mathbf{H}(\omega)$ is a lower triangular matrix with real and non-negative diagonal elements and with generally complex off-diagonal elements. After, $v(z, t)$ is computed as

$$v\left(z_i, t\right) = 2\sum_{k=1}^{n}\sum_{l=1}^{N_\omega}\left|H_{ik}(\omega_{kl})\right|\sqrt{\Delta\omega}\cos(\omega_{lk}t - \theta_{ik}(\omega_{kl}) + \Phi_{kl}) \tag{21}$$

with

$$\Delta\omega = \frac{\omega_{\text{cutoff}}}{N_\omega}; \quad \omega_{kl} = \left(l - \frac{N_\omega - l}{N_\omega}\right)\Delta\omega; \quad \theta_{ik}(\omega_{kl}) = \tan^{-1}\frac{\mathrm{Im}(H_{ik}(\omega_{kl}))}{\mathrm{Re}(H_{ik}(\omega_{kl}))} \tag{22}$$

where ω_{cutoff} is an upper bound cutoff frequency of the cross-spectral density matrix that can be taken as $\omega_{\text{cutoff}} = N\Delta\omega$.

In this study, three wind hazard levels are considered: frequent, occasional, and rare, corresponding to 10, 50, and 100 years mean recurrence intervals, with associated $\overline{V}_0$ = 32, 38, and 44 m/s in a suburban region, respectively.

Seismic loads are simulated using the set of six earthquake events used in [39]. The ground motion records are extracted from the PEER ground motion database. The design response spectrum is established following ASCE 7–16 [40] and based on the assumption that both buildings are in a site with S_{DS} = 1.01 and S_{D1} = 0.452. The selected ground motions are scaled to the structure's first fundamental period based on the amplitude-scaling method. The selected earthquakes along with scale factors are listed in Table 6 for both buildings and their corresponding scaled ground motion response spectra are plotted in Fig. 3.

Table 6
Selected earthquakes and corresponding scale factors.

Earthquake (year)	Magnitude	Station (component)	Distance	Scale factor	
			(km)	5-story	20-story
Manjil (1990)	7.37	Abbar (90°)	12.5	0.7	1.08
Imperial Valley (1979)	6.53	El Centro array #11 (140°)	13	1.63	1.08
Loma Prieta (1989)	6.93	Agnus State Hospital (0°)	24	2.275	1.57
Northridge (1994)	6.69	West Covina (315°)	51	3.2	4.16
Landers (1992)	7.28	Amboy (90°)	69	1.59	1.72
Kern County (1999)	7.36	LA-Hollywood Stor FF (90°)	115	2.7	1.85

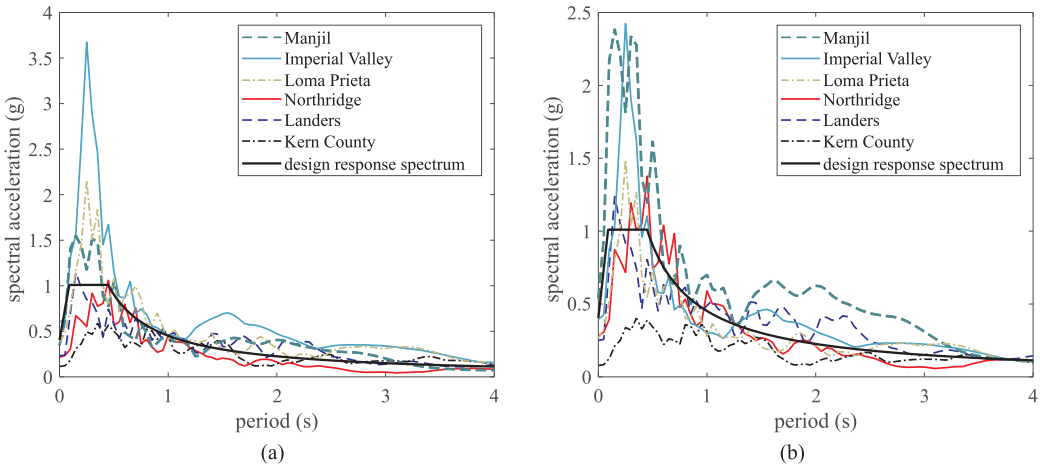

Fig. 3. Scaled seismic response spectrum of the selected earthquakes: (a) 5-story; and (b) 20-story building.

3.3. Performance objectives

The performance of the control systems is assessed following their capabilities to achieving specific performance objectives depending on the nature of the external excitation. These performance objectives are described in what follows. It is assumed for conciseness that performance criteria for wind-induced excitations are exclusively linked to discomfort caused by floor accelerations, and to low drift to maintain a fully elastic structural state under the studied wind hazards. Micheli et al. [41] defined a set of acceptable acceleration ranges based on different hazard levels and target performance objectives. In this study, it is assumed that the building should satisfy essential performance objectives corresponding to frequent, occasional, and rare wind hazard levels with acceptable acceleration ranges of 10–25 mg, 25–35 mg, and 35–45 mg, respectively. Moreover, the structure should remain elastic under all of the considered wind hazards. A 0.5% inter-story drift limit is considered to satisfy displacement constraints [42].

For seismic loadings, it is assumed that the performance is exclusively linked to structural damage caused by excessive inter-story drift, and while it is recognized that excessive acceleration is an important source of damage, acceleration-based performance is ignored for brevity. For a structure equipped with a supplemental damping system, it is generally desirable to design for no permanent damage under the design loads. An inter-story drift of 0.7% satisfies this requirement [42].

It is important to remark that the focus of the study is on the performance of the device at mitigating single load types with a single performance objective. In the case of multi-objective and/or multi-hazard applications, one would be required to perform a multi-objective optimization to obtain an optimal performance-based design of the supplemental energy dissipation system. This is left to future work.

3.4. PVFD design procedure

A typical damper design is conducted through an analytical motion-based design procedure, as described in [1]. However, given the highly customizable hysteresis of a typical PVFD combined with its highly nonlinear behavior, solutions are usually not mathematically trackable. Instead, a numerical design solution is applied. Using Eqs. (1)–(8), a set of representative hysteresis behaviors are generated to reduce the search space. These selected shapes for seismic and wind mitigation are plotted in Figs. 4(a) and (b), respectively. Table 7 lists the parameters used to generate the selected shapes along with the scaling factor N_p used in the numerical simulations. For seismic mitigation, given the primary control objective of interstory drift reduction, hysteresis shapes are selected such that the damping force increases with increasing displacement. For wind vibration mitigation, given the primary control objective of acceleration reduction, a set of more diverse hysteresis shapes are considered, some of which exhibit a decreasing trend in damping force with increasing displacement. To obtain better grounds for comparison, the geometric properties of the cams are tuned to obtain equal maximum forces at 0.7% and 0.5% inter-story drift ratios for seismic and wind loading, respectively, corresponding to the target drift ratios.

The tuning of the cam geometries is conducted through a scaling process. Because the parameters listed in Table 1 are drawn from an experimental setup with only one preloading case, and that the parameters of the LuGre model presented in Section 2 are highly dependent on the magnitude of the preloading force, they cannot be extended to model dampers with larger capacities. Instead, to numerically model PVFDs capable of proper capacities to meet the performance targets, the force output of the experimentally verified model is scaled by a factor termed damper multiplier N_m. To obtain the damper multipliers, it is assumed that the building is equipped with friction dampers with constant normal force (cam 1). Values of N_m for wind and seismic events are obtained through an iterative design procedure, yielding $N_m = 850$, and $N_m = 4000$ for the 5- and 20-story buildings, respectively, under seismic excitation and $N_m = 550$ for 20-story building under wind excitation.

For each building, there are $N_c^{N_s}$ possible permutations of cam profiles over the height of the structure, where N_c is the number of selected hysteresis loops and N_s is the number of floors. Because of a very large number of permutations in the case of the 20-story building, the search space is further decreased by dividing the building into four 5-story sections and assigning a single cam profile to a given section. It follows that there are 3125 and 625 possible permutations for the 5- and 20-story buildings, respectively.

A database of the buildings' responses is generated for and all the selected damper combinations. The geometric properties and scaling factors of these dampers are listed in Table 7. For each of the combinations, the maximum acceleration under wind loads, and maximum drift ratio of the building under seismic loads are obtained using the numerical model described in Section 3. A probabilistic analysis is then performed on the output data to quantify the performance of the system based on the selected cams. The probabilistic design framework is further discussed in Section 4.1 through a demonstration.

4. Results and discussion

A database of structural responses for each hazard level under different realizations is generated following the design procedure as described in Section 3.4. After, the optimal PVFD combination is selected

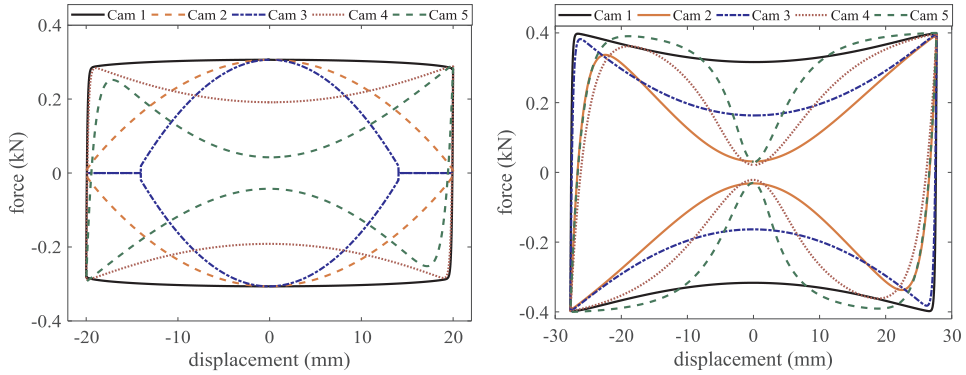

Fig. 4. The selected sets of representative hysteresis behaviors for (a) wind; and (b) seismic loadings.

Table 7
Geometric parameters of the selected sets of representative behavior.

Parameter	Cam (wind loading)					Cam (seismic loading)				
	1	2	3	4	5	1	2	3	4	5
a (mm)	40	38.5	38	41	43.5	40.2	45.5	40.7	43	44
b (mm)	40	40	40	40	40	40	40	40	40	40
d (mm)	28	60	55	50	28	40	28	28	10	10
N_p	1	1	1	0.55	0.15	1	0.1	0.45	0.08	0.06
F_{preload} (kN)	0.7	0.7	0.7	0.7	0.7	0.7	0.7	0.7	0.7	0.7

and its performance benchmarked against that of the uncontrolled building and of equivalent viscous and passive friction dampers.

4.1. Cam profile selection process

The cam profile selection process is first demonstrated on the 20-story building given the lower number of possible design permutations (i.e., simplest scenario). Design is conducted under rare wind hazard, and the building performance is later verified under frequent and occasional wind hazards.

A database of acceleration responses for each section of the 20-story building is constructed using 5 rare wind realizations. The maximum accelerations of the building under each realization and each selected damper combination are obtained from the database. After, the probabilistic distributions of accelerations are created to study the building performance under each cam profiles listed in Table 7 for a specific building section. Performance is assessed through a log-normal fit of the distributions and by evaluating the probability P of the maximum absolute acceleration $A_{\max}$ exceeding the acceleration threshold t_a

$$P\left(A_{\max} < t_a\right) = \Phi(t_a) = \int_0^{t_a} f_A(x)\mathrm{d}x \tag{23}$$

where $f_A(x)$ is the probability density function of a log-normal distribution with median μ and standard deviation σ, and $t_a = 45$ mg under rare winds. The cam yielding the best performance is selected, and the procedure is repeated for the structure equipped with that particular cam at that particular section. Here, the design starts at the base of the building and moves upwards. Fig. 5 shows an example of a fitted log-normal distribution with median μ and standard deviation σ for cam 1 fixed in Section 1 and with all possible variations of cams in the other sections. Four other distributions are generated for each cam in the first section and the best performance is selected. With the cam selected for the first section, similar distributions are created for the second section assuming the selected cam is fixed in the previous section.

The resulting design matrix is shown in Fig. 6. The rows of the matrix correspond to the wind loading cam profiles listed in Table 7.

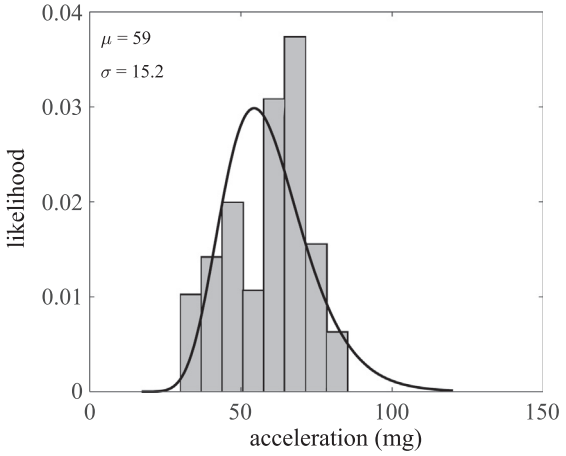

Fig. 5. Fitted log-normal distribution on maximum acceleration data for cam 1 fixed in section 1.

These profiles are fixed across the given sections (table columns) of the building. The first column of the distributions in the figure shows the distributions of acceleration responses of the building for a given cam profile (table rows) selected as fixed in Section 1. Results depicted in the first column show that the probabilities of the building experiencing accelerations lower than the target limit are 14%, 8%, 4%, 10%, and 7% under cam profiles 1 to 5, respectively. Cam 1 is selected as the one that yields the highest probability of mitigation vibrations. The second column in Fig. 6 plots the distributions of acceleration performance for each cam profile in Section 2 and taking cam 1 fixed in Section 1. Cam 1 yields the best performance with $\Phi(t_a) = 18\%$ for the second section. The process continues under Section 3 and Section 4 (cam 5 selected), providing the optimal combination cam 1, cam 1, cam 1, and cam 5 in Sections 1 to 4, respectively. The selected distributions are highlighted in the figure with green dashed rectangles. The higher performance provided by cam 5 in the top section of the building can be attributed to the relatively low drift of the upper floors, whereas a friction damper with high activation force would provoke higher accelerations. Generally, as observed in Fig. 6, for sections where the building motion can overcome the activation force (i.e., Sections 1–3), higher energy dissipation capacity correlates with lower acceleration, and for stories with low drifts, lower activation forces correlates with lower accelerations.

A similar procedure to cam profile selection for wind is followed for seismic excitation with the corresponding seismic cam profiles listed in Table 7, but with the probabilistic performance metric of interest taken as

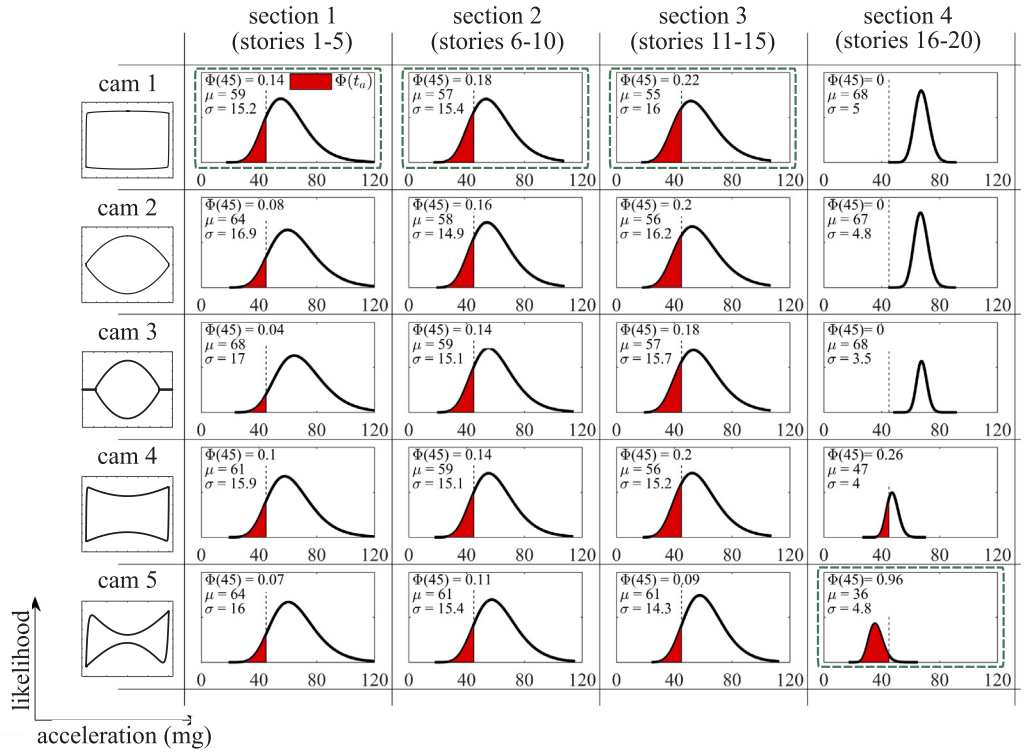

Fig. 6. Distributions of maximum absolute acceleration data caused by rare winds on the 20-story building.

$$P\left(D_{\max} < t_d\right) = \Phi(t_d) = \int_0^{t_d} f_D(x)\mathrm{d}x \tag{24}$$

where $D_{\max}$ is the maximum absolute inter-story drift, $t_d = 0.7\%$ is the drift threshold, and $f_D(x)$ is a log-normal distribution of median μ and standard deviation σ. In addition to designing for the performance target, the variation of the drift over the height of the structure is also considered for seismic loading in order to maintain a uniform drift and reduce risk of damage concentration. Fig. 7 shows the design matrix for the 5-story building, with σ_{drift} being the mean value of the standard deviation of drift over the height of the building. Because the drift limit is satisfied, the design is based on σ_{drift} instead of the expected value μ. Starting from the first story (column 1), all cam profiles satisfy the target drift but yet with cam 1 yielding the best performance in terms of drift variation. In the second story, taking cam 1 as fixed on the first story (column 2), cam 1 yields the best performance. Repeating the process leads to the following optimal configurations: cam 1, cam 1, cam 5, cam 5, and cam 2, for stories 1 to 5, respectively, as shown in the figure.

Lastly, Fig. 8 shows the design matrix for the 20-story building subjected to seismic excitations. Following the same procedure, the

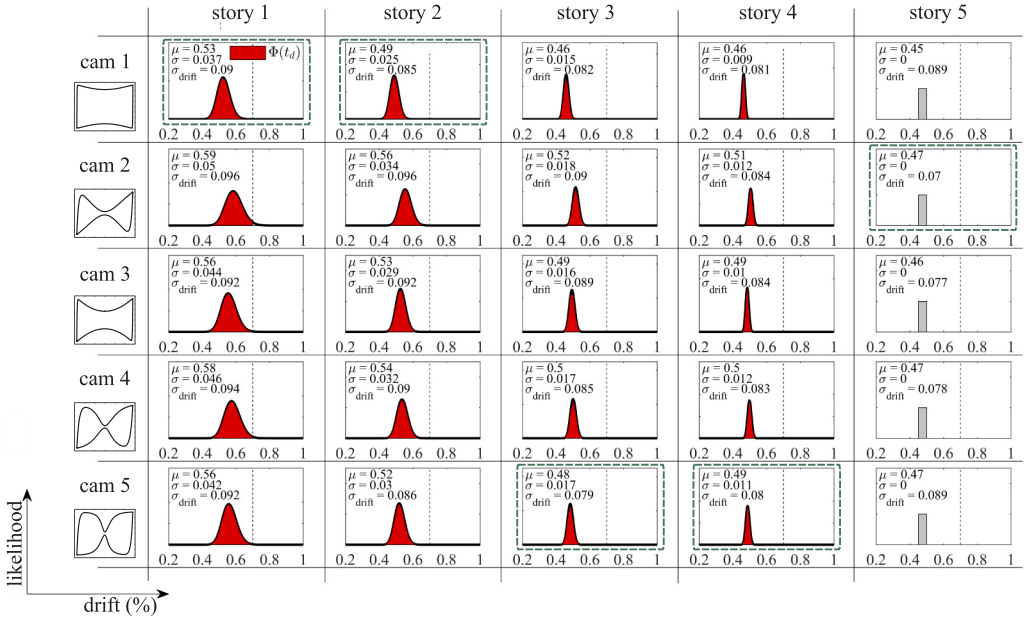

Fig. 7. Distributions of maximum absolute drift data caused by seismic excitations on the 5-story building.

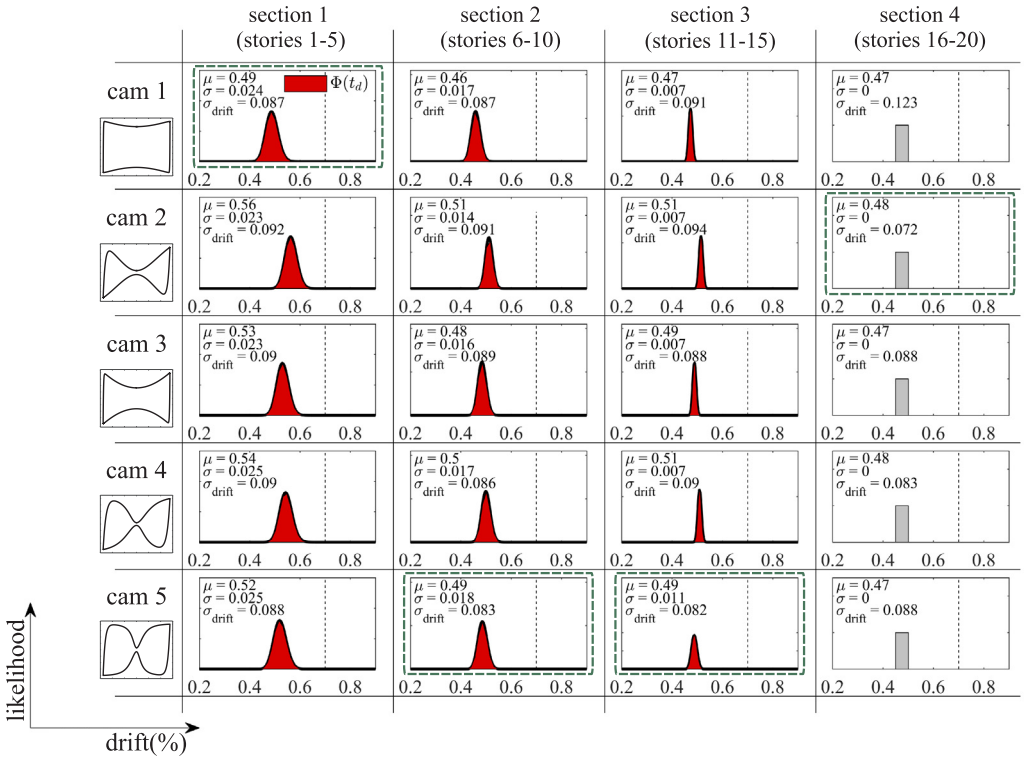

Fig. 8. Distributions of maximum absolute drift data caused by seismic excitations on the 20-story building.

resulting optimal combinations, highlighted in the figure by green dashed rectangles, are cam 1, cam 5, cam 5, and cam 2, for Sections 1 to 4, respectively.

The last column of the design matrix for earthquake loading is not a probability distribution. Unlike wind loading, where the data for each wind realization is used individually, in case of earthquake loading, the mean value of the maximum response under the earthquake suite is used because of the variability of responses under seismic excitation. Therefore, for the last cam, there would only be one combination per cam.

4.2. Performance evaluation

The performance of the selected cam profile combinations at mitigating natural hazards is evaluated under both example buildings by assessing the capability of the control method at restricting structural motion to target thresholds, and by comparing performance against equivalent viscous dampers and equivalent PFDs.

The equivalent viscous dampers and PFDs are designed by equating the energy dissipated by the PVFD under a harmonic load. The equivalent dampers are calculated as [1]

$$c_{\text{eq,viscous}} = \frac{\int_0^t F_{\text{PVFD}} u \, \mathrm{d}t}{\int_0^t \dot{u}^2 \, \mathrm{d}t} \tag{25}$$

$$F_{\text{max,PFD}} = \frac{\int_0^t F_{\text{PVFD}} u \, \mathrm{d}t}{\int_0^t \dot{u} \, \mathrm{d}t} \tag{26}$$

with

$$u = \hat{u}\sin(\omega t) \tag{27}$$

where $c_{\text{eq,viscous}}$, and $F_{\text{max,PFD}}$ are the equivalent viscous damping coefficient and the maximum force of the PFD, respectively, $\hat{u}$ is the amplitude of vibration taken as the target drift corresponding to each hazard level, and ω is the excitation frequency taken as the first natural frequency of the structures. Tables 8 and 9 list the parameters equivalent to each cam profile for both structures under wind and seismic loadings, respectively.

Table 8
Equivalent viscous damping coefficient and PFD maximum force - wind loading.

Cam	$c_{\text{eq,viscous}}$ (kN·s/m)	$F_{\text{max,PFD}}$ (kN)
1	9429	162
2	7976	137
3	6637	115
4	6491	112
5	2826	48

Table 9
Equivalent viscous damping coefficient and PFD maximum force - seismic loading.

	5-story		20-story	
Cam	$c_{\text{eq,viscous}}$ (kN·s/m)	$F_{\text{max,PFD}}$ (kN)	$c_{\text{eq,viscous}}$ (kN·s/m)	$F_{\text{max,PFD}}$ (kN)
1	3944	323	53009	1297
2	1124	92	18929	463
3	2308	189	32684	799
4	1669	137	28104	687
5	2441	200	39695	971

The performance of the building under wind excitations is evaluated using 50 wind realizations under each hazard level applied to the different control cases, in addition to the uncontrolled buildings. A normal distribution is fitted to the maximum accelerations of the building under wind loads. The distribution of the maximum acceleration under each control case is plotted in Fig. 9, which also shows the mean acceleration responses. Results show that the uncontrolled case does not satisfy the acceleration performance under any hazard levels, while the PVFD case yields satisfactory motion under each hazard level. The PVFD also outperforms the viscous case by resulting in relative gains of

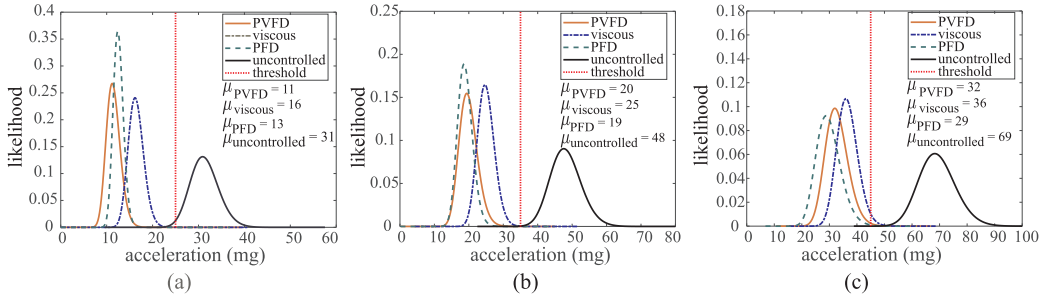

Fig. 9. Distributions of maximum absolute accelerations under each control case compared against uncontrolled for: (a) frequent; (b) occasional; and (c) rare wind hazards.

31%, 20%, and 11% in accelerations under frequent, occasional, and rare wind hazard levels, respectively. However, relative to the PFD, the PVFD only outperforms under the frequent wind hazard with a relative gain of 15% in acceleration, but underperforms under the occasional and rare wind events with relative losses of 5% and 10% in acceleration, respectively.

To further study the relative performance of the PVFD against that of the equivalent dampers, one can evaluate the number of times that the acceleration responses exceed a given threshold over an event, instead of relying on a single data point (i.e., the maximum absolute acceleration response). Here, the number of times that the absolute acceleration on the floor with the highest acceleration responses exceed 60% of threshold t_a, $N_{|\ddot{x}| > 0.6t_a}$, is counted. Metric $N_{|\ddot{x}| > 0.6t_a}$, a measure of how well a control system is successful at maintaining a smooth structural response, is evaluated under each hazard level over all 50 wind realizations. The threshold of 60% is selected arbitrarily to demonstrate a relatively narrow band of the acceleration response. The distribution of $N_{|\ddot{x}| > 0.6t_a}$ is plotted in Fig. 10 under each hazard level and control case. On average, $N_{|\ddot{x}| > 0.6t_a}$ is significantly lower for the PVFD compared against the two other passive damping schemes. Also, the building with the PVFD experiences significantly less variations in $N_{|\ddot{x}| > 0.6t_a}$ under different wind realizations, which signifies a more constant performance of the system. This higher performance of the PVFD can be attributed to the customization of the hysteresis. Fig. 11 plots the acceleration time histories of the top floor for a typical wind realization. A comparison of the enlarged sections shows that the PFD (Fig. Fig. 11(b)) tends to oscillate away from center, attributable to the larger activation force and causing a higher count $N_{|\ddot{x}| > 0.6t_a}$.

Another performance metric of interest is the drift ratio, which thus far has been assumed to be satisfied under rare wind loads. The drift target threshold is taken as 0.5% to satisfy the elastic limit [42]. Here, the satisfaction of the drift target is examined under the rare wind hazard events. Similar to the acceleration data, normal distributions are used to model the maximum drifts of the building with and without a controlled system, and is plotted in Fig. 12. The maximum drifts of the building are below the target level for all control cases. Compared to the uncontrolled case, the means of the maximum drifts are reduced by 30%, 36%, and 42% for PVFD, viscous, and PFD control cases, respectively. However, the use of the PVFD results in a higher average and spread of drift compared with the two other control schemes, with a negligible probability (0.58%) of exceedance of the design threshold.

The evaluation of the PVFD performance is continued for both buildings subjected to seismic excitations. The responses of the buildings equipped with the selected optimum PVFD combinations are plotted in Fig. 13 under the design level earthquake events. The performance target is satisfied for both buildings. One can observed that the drift distributions over the heights of both buildings, in particular for the 20-story building, are quite uniform. .

The performance of the PVFD is also compared against that of the other control devices. Fig. 14 plots the average drift profiles, taken by averaging the maximum absolute drifts over all earthquake realizations, for the building equipped with PVFD, viscous dampers, PFD, and uncontrolled. The figure also reports the average standard deviations of the drift over the height of the structure. The shaded areas in the figure show the bounds of the drift for each control case. All control cases significantly reduced the mean maximum drift of the uncontrolled building. Although the mean value of the drifts of all the control strategies are similar, in some loading cases, the maximum drift of the structure slightly exceeds the threshold for the viscous and PFD cases in the 5-story building and for the PFD in the 20-story building. Also, for both buildings, the PFDs exhibits a wider range of responses compared to the other two control strategies. In the case of the 20-story building, an inspection of the average standard deviations of the drift reveals that the PVFD strategy yields the most uniform drift in the response profile.

5. Conclusion

In this study, the performance of a novel passive variable friction device (PVFD) at mitigating wind and seismic loads was numerically assessed. The PVFD is a friction device designed to produce a damping force that varies as a function of its rotation through a customizable cam mechanism, resulting in a customizable friction hysteresis. The objective of the study was to assess the benefits of crafting the friction behavior to satisfy motion criteria. Due to the high nonlinearity of the

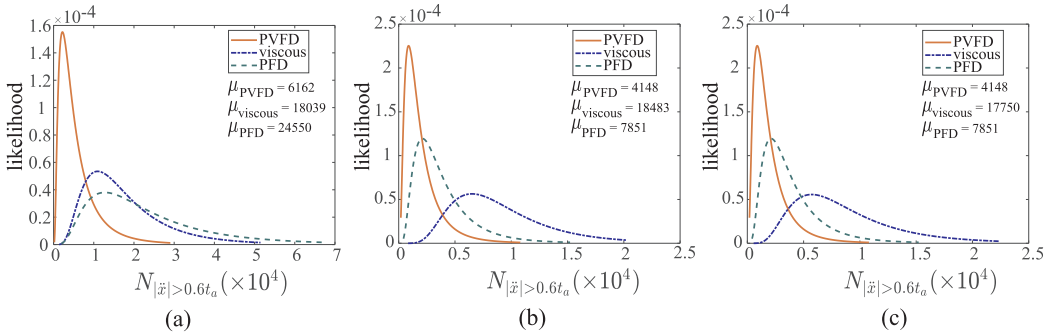

Fig. 10. Metric $N_{|\ddot{x}| > 0.6t_a}$ under each control case for: (a) frequent; (b) occasional; and (c) rare wind hazard.

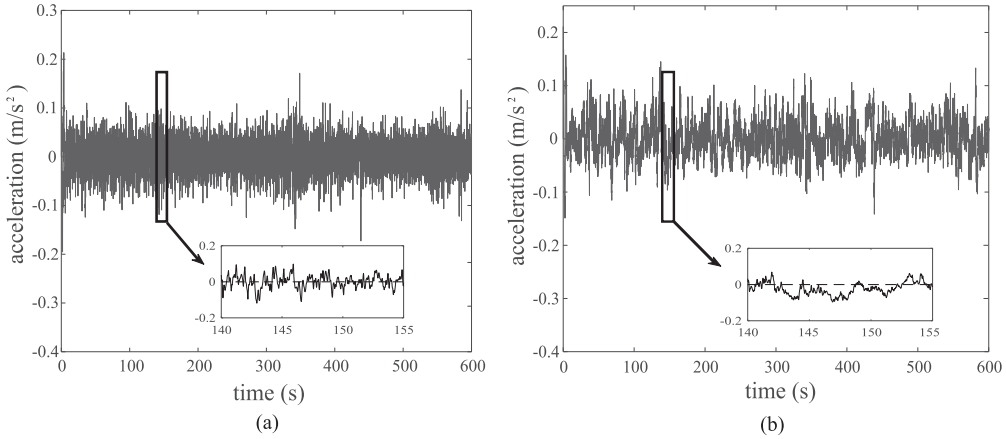

Fig. 11. Acceleration time history for a typical wind realization: (a) building equipped with PVFDs, (b) building equipped with PFDs.

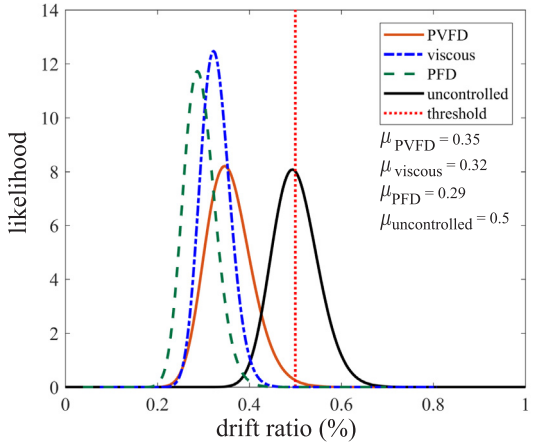

Fig. 12. Distribution of maximum drift for the 20-story building under rare wind hazards (50 wind realizations).

device resulting in mathematically non-trackable analytical solutions, a probabilistic approach was used to select an optimal damper configuration (i.e., hysteresis shapes) over the stories of the building. The approach consisted of producing a set of responses to different hazard realizations under various cam configurations, and sequentially selecting cams that resulted in the best performance and repeating the procedure by holding the selected cams constant. The performance metrics were the lowest expected maximum absolute acceleration for wind loads, and the lowest variation in inter-story drifts for seismic loads.

The proposed approach was demonstrated on a 5-story and a 20-story building subjected to wind and seismic loads. The effects of varying the hysteresis behaviors of the PVFD on the response of the selected buildings were presented and studied under a probabilistic framework. For the purpose of acceleration reduction, results show that hysteresis behaviors that equivalently reduce the stiffness of the structure are not effective, while hysteresis behaviors with high activation forces showed good performance, unless the inter-story movement was not large enough to activate the device in which case a lower activation force showed better performance. For the purpose of drift control, the results showed that utilizing dampers with the highest dissipation capacity did not yield optimal performance, and the optimal cam combinations consisted of a mix of different hysteresis shapes.

Simulation results demonstrated that the probabilistic framework identified a set of PVFDs that yielded desired performance under both wind and seismic excitations. The performance was compared against that of two equivalent damping schemes: passive viscous and passive friction dampers (PFDs). In the case of wind-induced vibrations, both PVFDs and equivalent PFDs were shown to be more effective than the equivalent viscous dampers. However, for the selected building, the PVFDs resulted in a significantly more stable response in terms of lower accelerations over the entire wind event. In the case of seismic-induced vibrations, all three damper configurations demonstrated comparable performance with the PFDs performing similarly to the PVFDs, but yet slightly outperforming the other two dampers in terms of drift reduction in the 5-story building. The PVFDs provided a more uniform drift for the 20-story building compared to the equivalent damping schemes. Overall, the results of this study show the capability and applicability of

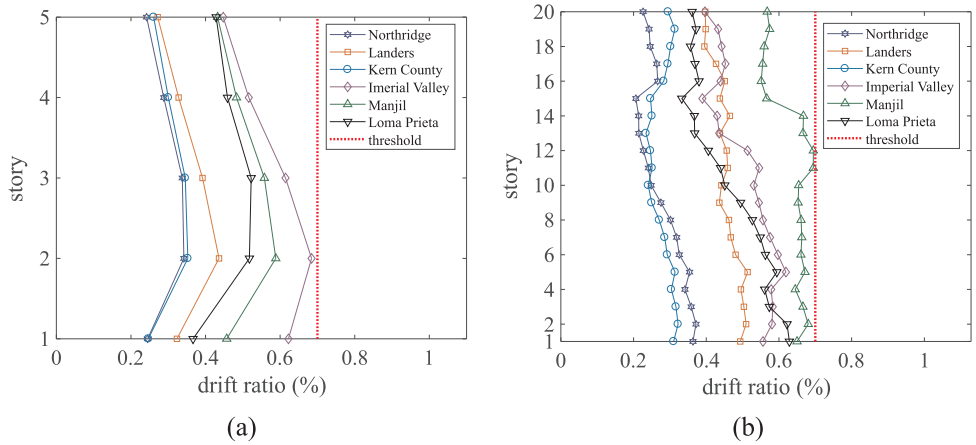

Fig. 13. Maximum drift distribution under design level earthquake: (a) 5-story; and (b) 20-story building.

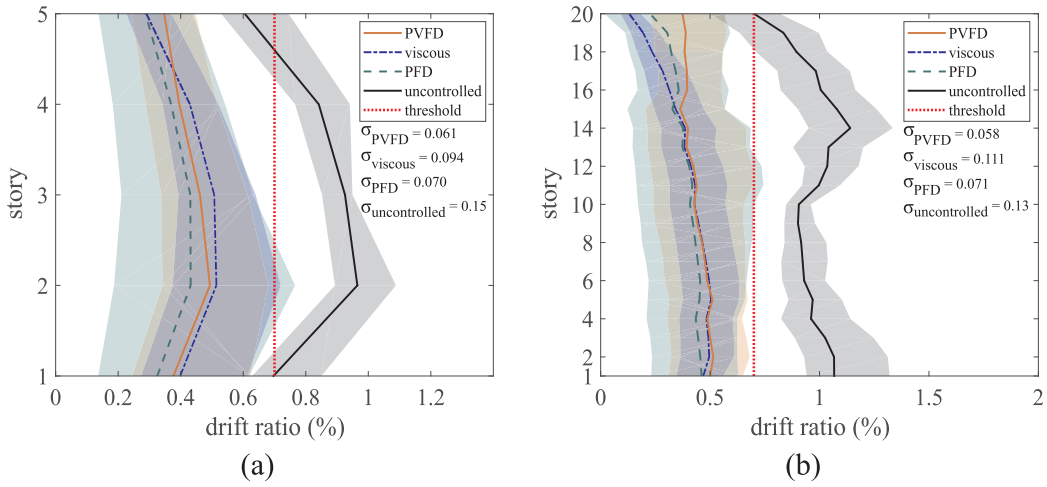

Fig. 14. Maximum drift distributions under seismic excitation of (a) 5-story, and (b) 20-story building.

the PVFD, which could empower designers with hysteresis customization capabilities in designing supplemental energy dissipation systems. The simple design of the PVFD also allows for the replacement of the cam in the advent of required modifications caused by damage or change in demand. For example, this can be useful to quickly update the supplement energy mitigation system to a permanent change in wind load arising from a change in cityscape.

CRediT authorship contribution statement

Vahid Barzegar: Conceptualization, Formal analysis, Investigation, Methodology, Validation, Writing - original draft, Writing - review & editing. **Simon Laflamme:** Conceptualization, Writing - original draft, Writing - review & editing. **Austin Downey:** Writing - review & editing. **Meng Li:** Investigation, Formal analysis, Writing - original draft, Writing - review & editing. **Chao Hu:** Writing - original draft, Writing - review & editing.

Declaration of Competing Interest

The authors declare that they have no known competing financial interests or personal relationships that could have appeared to influence the work reported in this paper.

Acknowledgment

The work presented in this paper is partially funded by the National Science Foundation under award numbers CMMI-1463252 and CMMI-1562992. Their support is gratefully acknowledged. Any opinions, findings, and conclusions or recommendations expressed in this material are those of the authors and do not necessarily reflect the views of the sponsor.

Appendix A. Supplementary material

Supplementary data associated with this article can be found, in the online version, at https://doi.org/10.1016/j.engstruct.2020.110920.

References

[1] Connor Jerome, Laflamme Simon. Structural motion engineering vol. 483. Springer; 2014.
[2] Soong TT, Spencer BF. Supplemental energy dissipation: state-of-the-art and state-of-the-practice. Eng Struct Mar 2002;24(3):243–59.
[3] Symans MD, Charney FA, Whittaker AS, Constantinou MC, Kircher CA, Johnson MW, et al. Energy dissipation systems for seismic applications: Current practice and recent developments. J Struct Eng Jan 2008;134(1):3–21.
[4] Edrees Saaed Tarek, Nikolakopoulos George, Jonasson Jan-Erik, Hedlund Hans. A state-of-the-art review of structural control systems. J Vib Control. 2013;21(5):919–37.
[5] Dong Baiping, Sause Richard, Ricles James M. Seismic response and damage of reduced-strength steel MRF structures with nonlinear viscous dampers. J Struct Eng Dec 2018;144(12):04018221.
[6] Puthanpurayil Arun M., Lavan Oren, Dhakal Rajesh P. Multi-objective loss-based optimization of viscous dampers for seismic retrofitting of irregular structures. Soil Dyn Earthq Eng. 2019:105765.
[7] Gong Shunming, Zhou Ying, Ge Pinglan. Seismic analysis for tall and irregular temple buildings: A case study of strong nonlinear viscoelastic dampers. Struct Des Tall Spec Build 2016;26(7):e1352.
[8] Pant Deepak R, Montgomery Michael, Christopoulos Constantin. Full-scale testing of a viscoelastic coupling damper for high-rise building applications and comparative evaluation of different numerical models. J Struct Eng 2019;145(2):04018242.
[9] Zhang Ruifu, Wang Chao, Pan Chao, Shen Hua, Ge Qingzi, Zhang Luqi. Simplified design of elastoplastic structures with metallic yielding dampers based on the concept of uniform damping ratio. Eng Struct 2018;176:734–45.
[10] Hashemi Ashkan, Clifton George Charles, Bagheri Hamed, Zarnani Pouyan, Quenneville Pierre. Proposed design procedure for steel self-centring tension-only braces with resilient connections. Structures 2020;25:147–56.
[11] Jarrah Majid, Khezrzadeh Hamed, Mofid Massood, Jafari Khashayar. Experimental and numerical evaluation of piston metallic damper (PMD). J Constr Steel Res 2019;154:99–109.
[12] Gutierrez Soto Mariantonieta, Adeli Hojjat. Tuned mass dampers. Arch Comput Methods Eng 2013;20(4):419–31.
[13] Love JS, Tait MJ. Multiple tuned liquid dampers for efficient and robust structural control. J Struct Eng 2015;141(12):04015045.
[14] Wang Wenxi, Dalton Dakota, Hua Xugang, Wang Xiuyong, Chen Zhengqing, Song Gangbing. Experimental study on vibration control of a submerged pipeline model by eddy current tuned mass damper. Appl Sci 2017;7(10):987.
[15] Okazaki T, Sato K, Sato E, Sasaki T, Kajiwara K, Ryan K, Mahin S. Nees/e-defense base isolation tests: perfomance of triple-pendulum bearings. 2012.
[16] Sun Tong, Lai Zhilu, Nagarajaiah Satish, Li Hong-Nan. Negative stiffness device for seismic protection of smart base isolated benchmark building. Struct Control Health Monit 2017;24(11):e1968.
[17] Anajafi Hamidreza, Medina Ricardo A. Comparison of the seismic performance of a partial mass isolation technique with conventional TMD and base-isolation systems under broad-band and narrow-band excitations. Eng Struct Mar 2018;158:110–23.
[18] Downey Austin, Cao Liang, Laflamme Simon, Taylor Douglas, Ricles James. High capacity variable friction damper based on band brake technology. Eng Struct Apr 2016;113:287–98.
[19] Pall Avtar S, Marsh Cedric. Response of friction damped braced frames. J Struct Eng 1982;108(9):1313–23.
[20] Mualla Imad H, Belev Borislav. Performance of steel frames with a new friction damper device under earthquake excitation. Eng Struct Mar 2002;24(3):365–71.
[21] Morgen B, Kurama Y. A friction damper for post-tensioned precast concrete beam-to-column joints. PCI J 2004;49(4):112–33.
[22] Wolski Michael, Ricles James M, Sause Richard. Experimental study of a self-centering beam–column connection with bottom flange friction device. J Struct Eng 2009;135(5):479–88.
[23] Miguel Letícia Fleck Fadel, Miguel Leandro Fleck Fadel, Lopez Rafael Holdorf. Simultaneous optimization of force and placement of friction dampers under seismic loading. Eng Optim 2015;48(4):582–602.
[24] Nabid Neda, Hajirasouliha Iman, Petkovski Mihail. A practical method for optimum seismic design of friction wall dampers. Earthq Spectra 2017;33(3):1033–52.
[25] Nabid Neda, Hajirasouliha Iman, Petkovski Mihail. Performance-based optimisation of RC frames with friction wall dampers using a low-cost optimisation method. Bull Earthq Eng 2018;16(10):5017–40.

[26] Ozbulut Osman E, Bitaraf Maryam, Hurlebaus Stefan. Adaptive control of base-isolated structures against near-field earthquakes using variable friction dampers. Eng Struct 2011;33(12):3143–54.
[27] Amjadian Mohsen, Agrawal Anil K. Vibration control using a variable coil-based friction damper. In Gyuhae Park, editor, Active and Passive Smart Structures and Integrated Systems 2017. SPIE, Apr 2017.
[28] Caudana Quintana H, Petkovski M. Optimum performance of structural control with friction dampers. Eng Struct. 2018;172:154–62.
[29] Panchal VR, Jangid RS. Variable friction pendulum system for near-fault ground motions. Struct Control Health Monit 2008;15(4):568–84.
[30] Calvi Paolo M, Moratti Matteo, Michele Calvi Gian. Seismic isolation devices based on sliding between surfaces with variable friction coefficient. Earthq Spectra. 2016;32(4):2291–315.
[31] Wang Gongxian, Wang Yangyang, Yuan Jianming, Yang Yi, Wang Dong. Modeling and experimental investigation of a novel arc-surfaced frictional damper. J Sound Vib 2017;389:89–100.
[32] Bagheri H, Hashemi A, Quenville P. Experimental test of a new self-centring tension-only brace using the resilient slip friction joint. Pacific Conference on Earthquake Engineering. 2019.
[33] Downey Austin, Sadoughi MohammadKazem, Cao Liang, Laflamme Simon, Hu Chao. Passive variable friction damper for increased structural resilience to multi-hazard excitations. In: Volume 2A: 44th Design Automation Conference. American Society of Mechanical Engineers, Aug 2018.
[34] Kurata Narito, Kobori Takuji, Takahashi Motoichi, Niwa Naoki, Midorikawa Hiroshi. Actual seismic response controlled building with semi-active damper system. Earthq Eng Struct Dyn 1999;28(11):1427–47.
[35] Gong Yongqiang, Cao Liang, Laflamme Simon, Ricles James, Quiel Spencer, Taylor Douglas. Motion-based design approach for a novel variable friction cladding connection used in wind hazard mitigation. Eng Struct 2019;181:397–412.
[36] Ohtori Y, Christenson RE, Spencer BF, Dyke SJ. Benchmark control problems for seismically excited nonlinear buildings. J Eng Mech 2004;130(4):366–85.
[37] Simiu Emil, Scanlan Robert H. Wind effects on structures: fundamentals and applications to design. 1996.
[38] Deodatis George. Simulation of ergodic multivariate stochastic processes. J Eng Mech 1996;122(8):778–87.
[39] Gong Yongqiang, Cao Liang, Laflamme Simon, Ricles James, Quiel Spencer, Taylor Douglas. Variable friction cladding connection for seismic mitigation. Eng Struct 2019;189:243–59.
[40] ASCE. Minimum Design Loads and Associated Criteria for Buildings and Other Structures (ASCE Standard - ASCE/SEI). American Society of Civil Engineers, 2017.
[41] Micheli Laura, Alipour Alice, Laflamme Simon, Sarkar Partha. Performance-based design with life-cycle cost assessment for damping systems integrated in wind excited tall buildings. Eng Struct 2019;195:438–51.
[42] Cha Young-Jin, Agrawal Anil K, Phillips Brian M, Spencer Billie F. Direct performance-based design with 200kn MR dampers using multi-objective cost effective optimization for steel MRFs. Eng Struct Jul 2014;71:60–72.